

MiPa: Mixed Patch Infrared-Visible Modality Agnostic Object Detection

Heitor R. Medeiros*, David Latortue*, Fidel Guerrero Pena,
Eric Granger, and Marco Pedersoli

LIVIA, Dept. of Systems Engineering, ETS Montreal, Canada

Abstract. In many real-world scenarios, using multiple modalities can greatly improve the performance of a predictive task such as object recognition. A common way of making use of multiple modalities is either by using "multimodal learning", in which multiple modalities are available for training and testing or by cross-modal learning, where one modality is used during training and another during testing. In this paper, we present a different way to use two modalities, in which either one modality or the other is seen by a single model. This can be useful when adapting an unimodal model to leverage more information while respecting a limited computational budget. This would mean having a single model that is able to deal with any modalities. To describe this, we coined the term anymodal learning. An example of this, is a use case where, surveillance in a room when the lights are off would be much more valuable using an infrared modality while a visible one would provide more discriminative information when lights are on. This work investigates how to efficiently leverage visible and infrared/thermal modalities for transformer-based object detection backbone to create an anymodal architecture. Our work does not create any inference overhead during the testing while exploring an effective way to exploit the two modalities during the training. To accomplish such a task, we introduce the novel anymodal training technique: Mixed Patches (MiPa), in conjunction with a patch-wise domain agnostic module, which is responsible of learning the best way to find a common representation of both modalities. This approach proves to be able to balance modalities by reaching competitive results on individual modality benchmarks with the alternative of using an unimodal architecture on three different visible-infrared object detection datasets. Finally, our proposed method, when used as a regularization for the strongest modality, can beat the performance of multimodal fusion methods while only requiring a single modality during inference. Notably, MiPa became the state-of-the-art on the LLVIP visible/infrared benchmark. Code: <https://github.com/heitorrapela/MiPa>.

1 Introduction

In recent years, the reducing costs in data acquisition and labeling have proportioned the advancements in multi-modality and cross-modality learning (Figure 1). Various fields are increasingly using this form of learning to enhance applications, such as surveillance [5], industrial monitoring [12], self-driving cars [22], and robotics [19], due to

* Equal contribution. Email: {heitor.rapela-medeiros.1, david.latortue}@ens.etsmtl.ca

their powerful ability to operate better in the presence of diverse environmental information [23]. For instance, the combination of visible and infrared has been showing promising results regarding such applications due to the changes in sunlight over the day that are highly minimized by the presence of multiple sensors [26].

In multimodal learning, the objective is to create a method able to incorporate multiple information from different sensors, whereas in cross-modality learning, it is rather to have one model able to use one modality for training and the other for evaluation, through an adaptation process. Although these classes of learning cover a wide range of applications, as aforementioned, we have identified an undesired scenario where one might want an all-weather/modality model that is trained on both modalities but is subjected to either one or another during inference. One example of that is a room under surveillance where the camera switches between modalities to address the need to make accurate detection in every lighting setting. We define a model able to support this situation as an **anymodal** model.

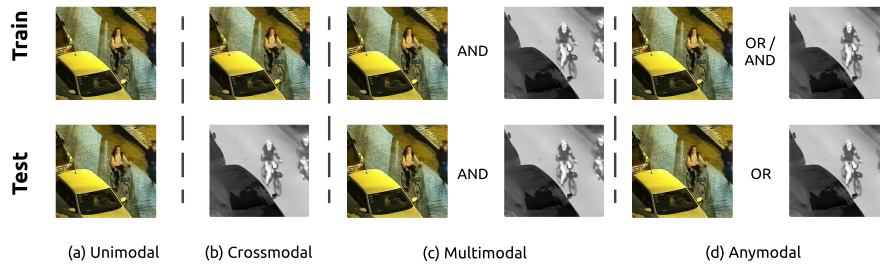


Fig. 1: Differences in inputs for different modality learning. (a) *Unimodal* learning assumes that only one modality is used for both training and testing. (b) *Cross-modal* assumes that one modality is used for training and another is used for testing. Thus, an adaptation is needed. (c) *Multimodal* learning requires multiple modalities and a special architecture to fuse them in order to improve performance. (d) *Anymodal* learning assumes that a model should be able to perform well for both modalities by using both for training but only one at a time for testing.

Despite the strong interest and business value in multimodal systems, much of the publicly available data and powerful pre-trained models are built around one modality: RGB. Furthermore, the lack of data for the infrared modality gives additional motives to build a detector upon an already pre-trained unimodal RGB detector. However, the current methods proposed in research to incorporate dual-modality information into a model require dedicated components associated with each modality, which makes them incompatible with such detectors. These methods are mainly fusion techniques that adopt modalities by either distributing the modalities across a four-channel, three of RGB followed by one for IR, input in the case of early fusion [25], merges both modalities later in the model architectures [4, 32, 33] in mid-stage fusion or ensembling different unimodal modality detectors [6] in late-stage fusion therefore, constraining the model to utilize both modalities during inference, increase significantly the parameter

count compared to a unimodal architecture and forego themselves from leveraging pre-trained detectors on the rich publicly available RGB datasets. In this work, we wanted to provide a way to train a model to be agnostic to its input modality yet still extract its knowledge during training to yield performances as good on both modalities as if it was trained solely on each during testing/production. The naive solution for this type of task is to train a model with a dataset that blends both modalities. Nonetheless, following this path may be obstructed by different challenge problems, such as modality imbalance [7] and alignment [2].

The emergence of the modern patch-based image classifiers catalyzed by the creation of ViT [8] as well as many works in the likes of Masked Autoencoders [11] and Multi-Modal Masked Autoencoders [1] have steered us towards exploring patch-based architectures to build a powerful and yet simple training technique to create a modality agnostic object detector. Such approaches have been promising for multi-modal learning, which allows an efficient combination of different information. This work investigates how to use visible and infrared modalities to build a **anymodal** object detector. This is done by using patch-based transformer feature extractors efficiently. Thus, Mi(xed) Pa(tch) does not introduce any inference overhead during the testing phase while exploring an effective way to use the two modalities during the training. To accomplish such a task, we introduce a non-deterministic complementary patch mixing method, allowing the detector to explore each modality without having to rely on both of them simultaneously. Subsequently, we enhance the training by suppressing the modality imbalances by proposing a modality-agnostic training technique, making the modalities indistinguishable from each other. This approach is designed to allow low-cost inference in production while removing all requirements of knowing beforehand which modality the detector is going to be used with. Hence, in applications that run the detector all day, we can know beforehand that any of the modalities, RGB or IR, whenever they are being used, are going to perform equally well.

Our work provides empirical results alongside a theoretical explanation based on information theory describing the benefits of using MiPa with transformer-based backbones. Additionally, we study the ability of our MiPa to also be used as a regularization method for the more robust modality to boost the overall performance of the detector and we even show that we can achieve state-of-art on the LLVIP benchmark. Finally, we also explore the compatibility of MiPa with convolutional-based models.

Our main contributions can be summarized as follows:

- (1) We introduce a novel anymodal method, MiPa, able to enhance the detection performance on each modality separately without increasing computational complexity during inference.
- (2) We show that the proposed method can also be used to improve the overall performance of detection when utilized as regularization for the strongest modality and achieve competitive results with multimodal fusion methods with less information during inference. For instance, such an approach achieved state-of-the-art results on thermal person detection in the LLVIP benchmark.
- (3) We empirically demonstrated that MiPa can simply be applied to any transformer-based backbones as well as detectors using these backbones.

2 Related Work

Patch-Based Image Classifier/ Feature extractor. With the integration of Transformers in the vision field, researchers have started to deconstruct images into patches to allow to modelling of long-range relationships between patches [8]. This powerful approach yielded great results and quickly became the norm amongst the top-performing models, ranking high and achieving state-of-the-art status on popular benchmarks such as ImageNet-1k [21]. Multiple variants of the vision transformer have been proposed in recent years: ViT [8], DEiT [24], SWIN [14], and VOLO [29] are some examples, just to name a few. Alongside the new way of utilizing input images came a novel pretraining method for image classification: Masked Autoencoders [11]. Indeed, this technique, which is simple to understand and easy to implement, consists of using a classifier as an encoder in an autoencoder architecture to generate images by only using a small fraction of the patches as input. This unsupervised method has proven to be very useful in terms of improving results in the finetuning stage. This idea has also been influential in the world of multi-modality models, when academics adapted it to their use case, by building a multimodal MAE with one encoder and multiple decoders to reconstruct all the different modalities [1]. The accolades of such classifiers motivated researchers to come up with ConvNeXt, a CNN built with an architecture akin to those of transformers [15]. Using this architecture enabled them to achieve similar results to Transformers while making the model compatible with the MAE pretraining to further boost performances [28]. Recently, researchers started using the SWIN Transformer as a backbone of DINO [30], an object detector descendant of the DeTr, and were able to become the state-of-the-art detector on the COCO detection benchmark [13].

Multi-Modal Visible-Thermal Object Detectors. Regarding object detection, the primary method of exploiting pairs of modalities, even when unaligned, are multimodal techniques; mainly fusion [3]. Fusion is a technique where we take advantage of multiple modalities in order to better optimize one training objective by combining them together to develop a multi-modal representation [17]. Fusion can be achieved at different stages of the inference, i.e., **early-stage fusion**, which concatenates the modalities across the channels, **mid-stage fusion**, where modalities are processed through dedicated decoders then merged e.g., Channel Switching and Spatial Attention (CSSA) [4], Halfway Fusion [32] or Guided Attentive Feature Fusion (GAFF) [33], and finally late-stage fusion, where typically modalities are processed independently through different models and combined at the end using ensembling [6] e.g. ProbEns [6]. The limitations of multimodal learning are that they require a custom architecture to handle each modality, are constrained to use both modalities during inference, and cannot use pre-trained weights from an unimodal detector. Anymodal models, however, are not affected by these limitations as the different modalities are only used during training. This type of architecture unlocks the ability for detectors to have a higher degree of freedom.

Modality Imbalance. A potential obstacle to a modality-agnostic network is the phenomenon of modality imbalance. Given a dataset with multi-modal inputs, modality imbalance occurs when a model becomes more biased towards the contribution of one modality [7] than the others. To counter that, several methods have been proposed, for

instance, gradient modulation [18], Gradient-Blending [27], and Knowledge Distillation from the well-trained uni-modal model [9]. In gradient modulation, Peng et al. proposed a mechanism to control the optimization of each modality adaptively by monitoring their contributions to the learning objective. In gradient blending, Wang et al. identified that multi-modal can overfit due to the increased capacity of the networks and proposed a mechanism to blend the gradients effectively [27]. Du et al. [9] show that training multi-modal-based models on joint training can suffer from learning inferior representations for each modality because of the imbalance of the modalities and the implicit bias of the common objectives in the fusion strategy.

3 Proposed Method

3.1 Preliminary definitions.

Let us consider a set of training samples $\mathcal{D} = \{(x_i, B_i)\}$ where $x_i \in \mathbb{R}^{W \times H \times C}$ are images with spatial resolution $W \times H$ and C channels. Here, a set of bounding boxes is represented by $B_i = \{b_0, b_1, \dots, b_N\}$ with $b = (c_x, c_y, w, h)$ being c_x and c_y coordinates of the bounding box with size $w \times h$. For the sake of simplicity, we omitted the class label of each bounding box from the notation. Then, in the training process of a neural network-based detector, we aim to learn a parameterized function $f_\theta : \mathbb{R}^{W \times H \times C} \rightarrow \mathcal{B}$, being \mathcal{B} the family of sets B_i and θ the parameters vector. For such, the optimization is guided by a loss function, which is a combination of a regression \mathcal{L}_{reg} and \mathcal{L}_{cls} term, i.e., l_2 loss and binary cross-entropy, respectively.

$$\mathcal{C}_{det}(\theta) = \frac{1}{|\mathcal{D}|} \sum_{(x,B) \in \mathcal{D}} \mathcal{L}_{cls}(f(x;\theta), B) + \lambda \mathcal{L}_{reg}(f(x;\theta), B). \quad (1)$$

Now, we want to train a model capable to perform well on two different modalities. While the naive way is to blend the two modalities during training, we will show in experimental results that that approach does not lead a balanced performance on both modalities. In the next section we present our proposed solution instead.

3.2 Mixed Patches (MiPa).

The MiPa training method is an anymodal training technique that leverages the patch input channel from transformer-based feature extractors to build a powerful common representation between modalities for the model. In short, it consists in sampling complementary patches from each modality and to rearrange the input into a sort of mosaic image (Figure 2). Such mechanism forces the model to see both modalities for each inference without being forced to have parameters specialized on a specific one. Depending on how the nature of the patches are sampled, the technique can act as a way to gather the union of information between both modalities or as a regularization for the strongest modality. Throughout this paper we will reference the sampling ratio as ρ . There a several ways to pick the sampling ratio ρ , the naive way of selecting ρ is to use a fixed ratio during the training of 50%. Then we can randomly generate a ρ value for

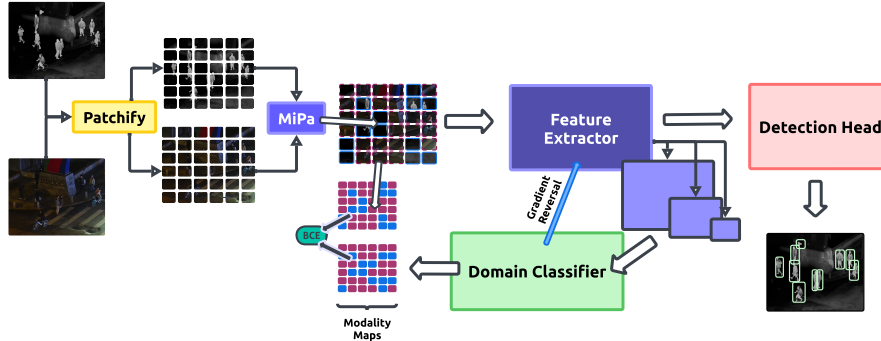


Fig. 2: Mixed Patches (MiPa) with Modality Agnostic (MA) module. In yellow is the patchify function. In purple is the MiPa module, then the feature extractor. In green the modality classifier, and in red the detection head.

each inference. If we have an intuition of which modality needs to be sampled more, we can manually move ρ during the training with a certain curriculum. Finally, we can let the model learn the optimal ratio by itself. In this work, we have explored all these techniques to see which one is the most suitable for MiPa.

Table 1: Definition of the random variables and information measures used to explain MiPa.

General		Functions	
Input scene in patches	\mathcal{X}_n	MiPa	\mathcal{M}
Number of patches	$n \in \mathbb{N}$	Self-Attention	SA
Patch id	$i \in \mathbb{N}$	Convolution	$C_k, k \in \mathbb{N}$
Random variables (RVs)		Modality channels	f, g
Patch ratio	$\rho \sim U(0, 1)$		
Patch channel f	$m \sim \binom{n-\rho}{p}, p = \frac{1}{2}$		
Patch channel g	$l \sim n - m$		
Information measures			
Entropy of V		$\mathcal{H}(V) := \mathbb{E}_{p_V} [-\log p_V(V)]$	
Information of X		Q, P where $Q = \mathcal{H}(q), P = \mathcal{H}(p)$	
Noise modality channels		η	
Mutual information between P and Q		$I(Q, P) = Q + P - Q \cap P$	
Approximation of mutual information between P and Q		$I_a \approx I$	

Theoretical explanation behind the MiPa approach. Here, we detail our theoretical understanding of the MiPa method. We refer to Table 1 for all definitions. The variable \mathcal{X} can be thought of as a scene where you would see individuals walking in a street for instance and the functions f and g are camera lenses capturing the information of the scene via IR and RGB respectively. The goal of MiPa (\mathcal{M}) is to make the learning more efficient by merging the information from both modalities and removing the redundancy between them while filtering the noise coming from each of them in a **single inference**.

Say we have:

$$f(\mathcal{X}) = P + \eta_f; g(\mathcal{X}) = Q + \eta_g$$

Then the application of \mathcal{M} can be summarized as the following equation:

$$\begin{aligned} \mathcal{M}(f(\mathcal{X}), g(\mathcal{X})) &= \begin{cases} f(\mathcal{X}_i), & i \in m \\ g(\mathcal{X}_i), & i \in l \end{cases} \\ &= (P_0 + P_1 + Q_2 + \dots + Q_{n-1} + P_n) + (m \cdot \eta_f + l \cdot \eta_g) \\ &= I_a + \eta \end{aligned} \quad (2)$$

The MiPa method is compatible with any patch-based feature extractor: which could be either a Transformer or a CNN. Nevertheless, the technique should work best alongside Transformer-based models. The transformer is made with a Self-Attention module while the CNN with convolutional layer. In the Self-Attention module, every patch contains the same channels, while in the patch-based convolution layer, the different neighboring patches go through their respective convolution kernel. In the case of the Self-Attention, the full approximation of I is fed to it:

$$SA(I_a + \eta),$$

but for the convolution kernels, fractions of I_a corresponding to each kernels are sent to each of them, such as in the following:

$$\begin{aligned} I_a &= I_{a1} + I_{a2} + \dots + I_{ak} + \eta \\ &C_i(I_a i + \eta) \end{aligned}$$

Consequently, each kernels get a poorer/inferior approximation of I . To verify that hypothesis, we are comparing the results from the pure MiPa in conjunction with ConvNeXt versus SWIN. Though MiPa ConvNeXt is expected to be outperformed by SWIN, the next section will detail how the Modality Agnostic module helps decreasing the performance gap between the modalities.

3.3 Patch-Wise Modality Agnostic Training.

As previously mentioned, modality imbalances can potentially cause the model to rely mostly on one modality. Since the objective of the this work is to preserve the original architecture of the model for inference, we opted for an approach where the backbone

would have the responsibility of mediating the modalities. To do so, we designed an adaption of the gradient reversal layer technique [10] called *patch-wise modality agnostic training*. The key idea is to prevent the detector from relying too much on the strongest modality to make its predictions by making the features from each modality indistinguishable. Considering that the input has a different modality for each patch, modality that we pick during the patch mixing process, we build what we call a *modality map*, denoted as M , that specifies which modality each patch belongs to for each inference during training. Then, we use a modality classifier to predict the modality map of the features coming from the backbone. Finally, we compute the loss between the target and outputted modality maps and back-propagate the opposite gradients to the backbone. To reduce the noise coming from the classifier at the beginning of the training, we slowly increase the weight (λ) of the gradients propagated to the backbone as the training goes on. We use the binary cross entropy to compute the loss between the predicted and target modality maps, as described by the following Equation (3):

$$\mathcal{L}_{ModInv}(\hat{M}, M) = \frac{1}{n} \sum_{i=1}^n -M \log(\hat{M}) - (1 - M) \log(1 - \hat{M}), \quad (3)$$

where M is the modality map generated from ρ . The aforementioned approach for the full training pipeline can be seen in Figure 2. We use the following Equation (4) to increment the factor λ .

$$\lambda = \frac{2}{1 + \exp(-\gamma s)} - 1, \quad (4)$$

where γ is the speed to which λ increases. The modality classifier can be used at any stage of the backbone; we have found experimentally that using it on the features from the stage 1 works well.

4 Results and Discussion

4.1 Experimental Setup and Methodology

Datasets. During our experiments, we explored three different multimodal benchmarking datasets with RGB and infrared modalities (LLVIP, FLIR, and KAIST).

LLVIP: The LLVIP dataset is a surveillance dataset composed of 12,025 IR and 12,025 RGB paired images for training and 3,463 IR and 3,463 RGB paired images for testing. The original resolution is 1280 by 1024 pixels but was resized to 640 by 512 to accelerate the training. The sole annotated class of this dataset is pedestrians. **FLIR ALIGNED:** For the FLIR dataset, we used the sanitized and aligned paired sets provided by Zhang et al. [31], which has 4,129 IRs and 4,129 RGBs for training, and 1,013 IRs and 1,013 RGBs for testing. The FLIR images are taken from the perspective of a camera in the front of a car, and the resolution is 640 by 512. It contains annotations of bicycles, dogs, cars, and people. It has been found that for the case of FLIR, the "dog" objects are inadequate for training [4], but since our objective is to evaluate if our method can make a detector modality agnostic and not beat any prior benchmark, we have decided to keep it. **KAIST:** The last dataset used to benchmark

our method is KAIST. Just like FLIR, it is also taken from the perspective of the front of a car. For KAIST, we used the set 20, which has 2,500 Thermal and 2,500 RGB images of a resolution of 640 by 480. The dataset contains classes of person, people, cyclist. Usually, the log miss rate [25] [33] [32] is the chosen metric to evaluate detectors on this dataset; however, to be consistent with our other benchmarks, we reported the mAP. For the case of KAIST, all the unimodal baselines diverged when evaluated on the testing set; therefore, since we evaluated the efficiency of our method, we considered the validation set instead. Thus, we do not compare this dataset’s performance with that of other papers. So, we opted to move the results of KAIST to the supplementary materials.

Training regiment. All our detectors were trained on an A100 NVIDIA GPU and were implemented using PyTorch. We use AdamW [16] as optimizer with a learning rate of $1e^{-4}$, a batch size of 6, and for a total of 12 epochs for the case of the DINO detectors and $1e^{-5}$ with a batch size of 8 and 50 epochs for Deformable DeTr. For both SWIN and ConvNeXt with the use of pre-trained weights from ImageNet [21]. We evaluated the models in terms of performance mAP_{50} , and we additionally reported the others mAP_{75} and mAP in the supplementary material. Furthermore, the evaluation is done in terms of RGB performance, IR performance, and our target metric, the mean average of both, because the anymodal setup requires a modal that is equally good on both modalities during test time.

4.2 Baselines

In the course of this work, we considered different baselines to compare to our proposed method (MiPa). Firstly, we measure the performance of the detector trained on one modality, uni-modal setup, to gain a reference of the expected detection coming from each modality. Secondly, we evaluate the naive solution of simply using a dataset comprised of both modalities during training. To account for the modality imbalances and further increase the fairness of our comparisons, we balanced the datasets with 25%, 50%, and 75% of one modality and the rest of the other. All models were evaluated separately on RGB and IR. Additionally, the mean of the modalities, which represents how well the model is balanced for the two desired modalities, is calculated.

4.3 Towards the optimal ρ

Since the way of selecting the ideal ρ was not clear, we designed different experimental settings to study the influence of ρ on learning the best way to balance the amount of IR/RGB information during the training. Let us start with a few definitions.

Fixed ρ . In the fixed setting, we selected a fixed amount of proportion between IR/RGB sampling, such as 0%, 25%, 50%, 75% and 100%, in which 0% correspond to none IR at each batch, and 100% correspond to only IR on the training batch.

Variable ρ . In the variable ρ , the ratio of mixed patches per batch is drawn from a uniform distribution. For each batch, a different ρ is redrawn.

Table 2: Comparison of different ratio ρ sampling methods on LLVIP

Modality	RGB	IR	AVG
Model	\mathbf{AP}_{50}	\mathbf{AP}_{50}	\mathbf{AP}_{50}
Fixed [$\rho=0.25$]	78.9	98.2	88.55
Fixed [$\rho=0.50$]	73.0	97.6	85.30
Fixed [$\rho=0.75$]	77.4	97.5	87.45
Variable	88.5	97.5	93.00
Learnable	69.8	97.0	83.40
Curriculum ($\rho=0.25$ for 8 epochs; then variable)	80.1	97.8	88.95
Curriculum ($\rho=0.25$ for 4 epochs; then variable)	76.6	97.8	87.20

Learnable ρ . In the variable ρ , the ratio of mixed patches per batch is drawn from a normal distribution with $\mu = 0.0$ and $\sigma = 1.0$. We then learn the optimal ρ by using the reparametrization trick. To prevent ρ from pushing from the strongest modality, we backpropagate an adversarial loss/reversed gradients.

Curriculum ρ . For the curriculum strategy, we tested different times during the training to give different importance to one modality over the other. For instance, during the initial epochs over the training, the model focuses on the weak modality, providing between 0% to 25% of ratio for IR, and then over the rest of training, it samples from the uniform distribution such as variable ρ .

We tested all the different configurations of ρ on LLVIP (see Table 1). For this experiment, we have made two findings. First, using an I_a following a uniform distribution gives us a better approximation of the range of information from $IR \cup RGB$ as the results from the variable give us a better balance between both modalities. Second, using less of the weaker modality strengthens the learning of the strongest one, as it can be seen in our table that we were actually able to beat the state of the art by sampling 25% or RGB images and 75% of IR.

4.4 Should MiPa work with convolutions?

As previously discussed, we were interested in the capacity of MiPa to work well alongside a convolution layer. To do so, we used the same exact training setup as for the transformer but replaced the backbone with ConvNeXt large [15] from torchvision pretrained on ImageNet22k [21]. As can be seen in the Table 4, ConvNeXt MiPa is short to beat all baselines by one in the case of Dino ConvNeXt on LLVIP and on FLIR and is under almost every baseline on KAIST. Therefore, as anticipated in our theoretical modeling of MiPa, we conclude convolutions are indeed not a suitable alternative for MiPa. Furthermore, the best performances were over the SWIN backbone, described in Table 3.

4.5 Patch-wise Modality Agnostic Training.

The subsequent ablation shows the efficacy of the patch-wise modality agnostic method towards obtaining a single model capable of dealing with both modalities while keeping

Table 3: Comparison of detection performance over different baselines and MiPa for different models on SWIN backbone. The evaluation is done for RGB, Thermal, and the average of the modalities.

		Dataset: LLVIP (AP ₅₀ ↑)			
Model	Backbone	Modality	RGB	Thermal	Average
DINO	SWIN	RGB	90.87 ± 0.84	94.23 ± 0.57	92.55
		THERMAL	66.87 ± 0.90	96.87 ± 0.12	81.87
		BOTH [$\rho = 0.25$]	79.73 ± 1.03	97.40 ± 0.22	88.57
		BOTH [$\rho = 0.50$]	82.40 ± 1.50	96.50 ± 0.29	89.45
		BOTH [$\rho = 0.75$]	81.23 ± 2.89	97.07 ± 0.25	89.15
		MiPa (Ours)	88.70 ± 0.45	96.97 ± 0.26	92.83
		MiPa + MI (Ours)	89.10 ± 0.28	96.83 ± 0.09	92.90
		Dataset: FLIR (AP ₅₀ ↑)			
Model	Backbone	Modality	RGB	Thermal	Average
DINO	SWIN	RGB	66.07 ± 0.98	56.60 ± 0.80	61.33
		THERMAL	56.47 ± 0.79	70.40 ± 0.38	63.43
		BOTH [$\rho = 0.25$]	56.53 ± 0.76	67.57 ± 1.73	62.05
		BOTH [$\rho = 0.50$]	60.50 ± 0.66	68.93 ± 0.60	64.72
		BOTH [$\rho = 0.75$]	58.53 ± 0.92	70.43 ± 0.65	64.48
		MiPa (Ours)	63.53 ± 1.94	69.50 ± 1.84	66.52
		MiPa + MI (Ours)	64.80 ± 2.30	70.43 ± 0.53	67.62
Def.DETR	SWIN	RGB	49.33 ± 1.39	43.77 ± 0.56	46.55
		THERMAL	39.17 ± 1.48	59.20 ± 0.29	49.18
		BOTH [$\rho = 0.25$]	35.73 ± 4.95	43.00 ± 13.54	39.37
		BOTH [$\rho = 0.50$]	33.93 ± 5.15	43.33 ± 14.14	38.63
		BOTH [$\rho = 0.75$]	32.90 ± 3.54	44.13 ± 14.85	38.52
		MiPa (Ours)	48.00 ± 0.57	54.97 ± 0.90	51.48
		MiPa + MI (Ours)	48.27 ± 1.24	55.80 ± 0.42	52.03

Table 4: Comparison of detection performance over different baselines and MiPa for different ConvNeXt. The evaluation is done for RGB, Thermal, and the average of the modalities.

		Dataset: LLVIP ($AP_{50} \uparrow$)		
Model Backbone	Modality	RGB	Thermal	Average
DINO ConvNeXt	RGB	90.77 ± 0.34	92.20 ± 0.62	91.48
	THERMAL	63.23 ± 9.02	95.60 ± 0.45	79.42
	BOTH [$\rho = 0.25$]	76.70 ± 4.04	96.27 ± 0.48	86.48
	BOTH [$\rho = 0.50$]	81.40 ± 2.55	95.50 ± 0.57	88.45
	BOTH [$\rho = 0.75$]	79.80 ± 1.49	95.60 ± 0.57	87.70
	MiPa (Ours)	81.03 ± 0.74	96.43 ± 0.12	88.73
		Dataset: FLIR ($AP_{50} \uparrow$)		
Model Backbone	Modality	RGB	Thermal	Average
DINO ConvNeXt	RGB	52.77 ± 1.43	48.33 ± 1.87	50.55
	THERMAL	39.43 ± 0.39	58.87 ± 0.87	49.15
	BOTH [$\rho = 0.25$]	45.87 ± 1.14	54.53 ± 1.20	50.20
	BOTH [$\rho = 0.50$]	48.00 ± 2.87	55.40 ± 0.05	51.70
	BOTH [$\rho = 0.75$]	52.97 ± 3.03	57.53 ± 0.86	55.25
	MiPa (Ours)	46.17 ± 0.66	56.27 ± 0.33	51.22

the performance stable. In Table 5, we studied the sensibility of the model performances influenced by different γ hyperparameters, seen in Equation (4), which tunes the speed to which the λ factor increases at each step the weight of gradients propagated to the feature extractor. We empirically demonstrate that the optimal γ varies between datasets and detectors due to the number of epochs required for each one, whereas if the model requires more training epochs, the γ should be higher. In the supplementary material, we provide additional curve plots related to the value of γ regarding the number of epochs.

Table 5: Comparison of detection performance over different baselines and MiPa for different models and backbones. The evaluation is done for RGB, Thermal, and the average of the modalities.

Model Backbone	Modality	Dataset: FLIR ($AP_{50} \uparrow$)		
		RGB	Thermal	Average
DINO SWIN	RGB	66.07 \pm 0.98	56.60 \pm 0.80	61.33
	THERMAL	56.47 \pm 0.79	70.40 \pm 0.38	63.43
	BOTH [$\rho = 0.25$]	56.53 \pm 0.76	67.57 \pm 1.73	62.05
	BOTH [$\rho = 0.50$]	60.50 \pm 0.66	68.93 \pm 0.60	64.72
	BOTH [$\rho = 0.75$]	58.53 \pm 0.92	70.43 \pm 0.65	64.48
	MiPa	63.53 \pm 1.94	69.50 \pm 1.84	66.52
	MiPa [$\gamma = 0.05$]	64.80 \pm 2.30	70.43 \pm 0.53	67.62
	MiPa [$\gamma = 0.10$]	64.03 \pm 2.11	69.63 \pm 1.45	66.83
	MiPa [$\gamma = 0.15$]	64.27 \pm 0.47	69.93 \pm 1.02	67.10
	MiPa [$\gamma = 0.20$]	61.83 \pm 1.39	69.27 \pm 1.57	65.55
	MiPa [$\gamma = 0.30$]	62.20 \pm 2.49	67.47 \pm 2.04	64.83
	MiPa [$\gamma = 0.40$]	61.13 \pm 2.88	67.93 \pm 0.92	64.53

4.6 Main Comparative Results.

Finally, in this section, we compare our approach in terms of performance with other methods in the literature concerning the detection performance of some traditional object detection on thermal and visible images. In Table 6, we can see that MiPa outperforms the competitors over FLIR and LLVIP. For instance, on FLIR, MiPA has 81.3 AP_{50} , while CSAA [4] has 79.2, ProbEns [6] has 75.5, GAFF [33] 74.6 and Halway Fusion [31] 71.5, a similar trend is seen in the other AP’s, which are reported on supplementary material. Furthermore, we report competitive results on LLVIP, which can be seen as the state-of-art thermal people detection performance over different benchmarks inclusively; both modalities are used during training and inference, which is not our case (as we just use the IR modality in this comparison for inference). Even though

Table 6: Comparison with different multimodal works on RGB/infrared benchmarks.

Method	Dataset					
	FLIR			LLVIP		
	AP ₅₀	AP ₇₅	AP	AP ₅₀	AP ₇₅	AP
Halfway Fusion [31]	71.5	31.1	35.8	91.4	60.1	55.1
GAFF [33]	74.6	31.3	37.4	94.0	60.2	55.8
ProbEns [6]	75.5	31.8	37.9	93.4	50.2	51.5
CSAA [4]	79.2	37.4	41.3	94.3	66.6	59.2
CFT [20]	78.7	35.5	40.2	97.5	72.9	63.6
MiPa (Ours)	81.3	41.8	44.8	98.2	78.1	66.5

we tried to be fair in the comparison, we want to clarify that each model has its own backbone.

5 Conclusion

In this work, we have introduced an **anymodal** training method leveraging patch-based transformer feature extractors to consolidate the mutual information between different modalities. This method, named MiPa, has enabled several object detectors to achieve **modality invariance** on several datasets without having to make any changes to their architecture or increase the testing inference time. Notably, MiPa DINO-SWIN was able to reach the performances on both modalities of LLVIP of its baselines, respectively, trained solely on each modality. Additionally, MiPa outperformed competitors on the LLVIP and became SOTA. Furthermore, we provide a definition from information theory regarding the knowledge captured by the MiPa method and why the models based on ConvNeXt were not as good as the ones from the SWIN backbone. In future works, we plan on exploring different strategies for the initial pre-train, such as masked autoencoders, and additionally understand at which points we can apply curriculum learning for balancing the modalities while exploring the complementary information of the modalities.

Acknowledgments: This work was supported by Distech Controls Inc., the Natural Sciences and Engineering Research Council of Canada, the Digital Research Alliance of Canada, and MITACS.

Supplementary Material: MiPa: Mixed Patch Infrared-Visible Modality Agnostic Object Detection

Heitor R. Medeiros*, David Latortue*, Fidel Guerrero Pena,
Eric Granger, and Marco Pedersoli

LIVIA, Dept. of Systems Engineering, ETS Montreal, Canada

In this supplementary material, we provide additional information to reproduce our work. The source code is provided alongside the supplementary material, and we are going to provide the official repository. This supplementary material is divided into the following sections: Additional visualizations (Section 1), Detailed diagrams (Section 2), Towards the optimal ρ (Section 3), Ablation on γ (Section 4) and MiPa on different backbones (Section 5).

1 Additional visualizations

In this section, we offer additional qualitative insights into detection performance across different times of the day. Specifically, we provide results for both day and night scenarios using various methods. In Figure 1, we highlight the advantages of employing MiPa for anymodal detection. For instance, MiPa exhibits fewer false positives than others while excelling in RGB detection. This superiority in RGB detection is not observed when training with both modalities jointly, where the dominance of the stronger modality, infrared, influences the learning process negatively.

2 Detailed diagrams

In this section, we provide additional diagrams aimed at enhancing the comprehension of both the baselines and our method in more detail. In Figure 2, we show the traditional strategy for constructing a multimodal model utilizing patches. First, the framework divides the images from both modalities (RGB and IR) into patches (purple block). Subsequently, the extracted patches are fed into the backbone of the model (depicted in blue).

In Figure 3, we present the proposed mix patches diagram. Similar to the previous diagram, we initially apply the patchify function (in purple), followed by the mix patches function (depicted in pink). This function receives the patches and performs a mix operation, such as sampling the patches from both modalities according to a uniform distribution. Finally, depicted in blue, is the backbone, while the detection head is highlighted in green.

Lastly, we provide an overview of an implementation of MiPa with DINO in Figure 4. While the image is similar to the previous one, we offer additional visualizations

* Equal contribution. Email: {heitor.rapela-medeiros.1, david.latortue}@ens.etsmtl.ca



Fig. 1: Detection over different methods for two different daytimes: Night and Day. Detectors trained on *RGB* works better at daytime. Detectors trained on *IR* work better at nighttime. Detectors trained on *BOTH* modalities cannot work well on any of them. Our *MiPa* manages to work well in both daytime conditions.

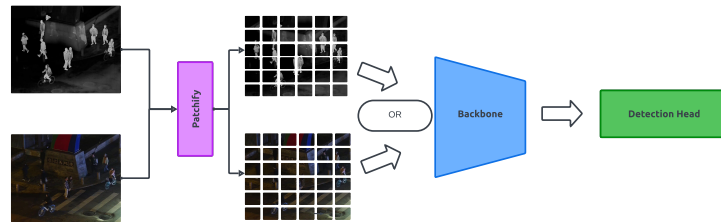


Fig. 2: Baseline for multimodal object detection learning with patches.

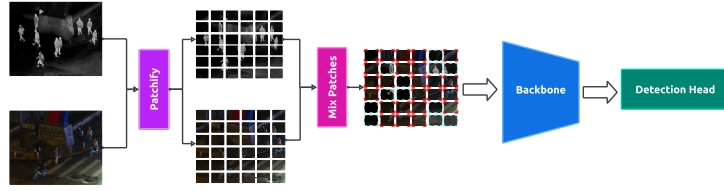


Fig. 3: Mix Patches diagram: First, in purple, is the patchify function, which is responsible for providing the patches. Second, in pink, is the mix patches function, responsible for mix the patches based on a pre-defined policy, e.g., uniform distribution of both modalities. Then, in blue, is the backbone and in green is the detection head.

showcasing the SWIN backbone alongside the modality classifier. For the sake of simplicity and to emphasize the MiPa’s modality classifier and the patchify/mix patches components, we omit the detection head in the figure.

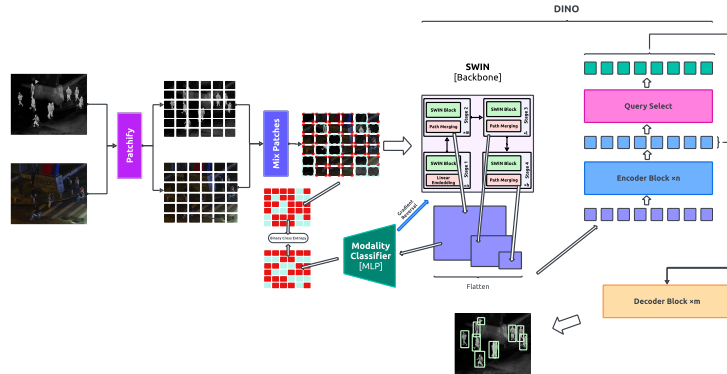


Fig. 4: MiPa with DINO: First, in purple, is the patchify function, which is responsible for providing the patches. Second, bold blue is the mixing patches function, which is responsible for mixing the patches based on a pre-defined policy, e.g., uniform distribution of both modalities. Then, we have the DINO alongside the modality classifier head for the GRL.

3 Towards the optimal ρ

In this section, similar to the main manuscript, we provide the study of various strategies devised within this work to find the optimal approach to select the parameter ρ .

Such a parameter represents the proportion of one modality, IR in our context, sampled during the training to facilitate optimal learning. As shown in Table 1, the variable strategy yields the most favorable results in terms of providing the optimal ρ . This effectiveness is attributed to the inherent characteristics of MiPa to act as a regularizer for the weaker modality, which is the RGB in our setup. Thus, as described, the variable strategy is the method that reached the best average across all the different APs. For example, the variable strategy was able to reach 88.5 AP₅₀ in RGB, outperforming other strategies. Although its performance in IR was slightly lower than that of the Fixed strategy [$\rho = 0.25$] (achieving 97.5 AP₅₀), the variable strategy’s overall mean performance was superior with 93.00 AP₅₀. This trend is similar to the other AP metrics, in which the RGB was improved, and the mean performance was better with the variable strategy.

Table 1: Comparison of different ratio ρ sampling methods on LLVIP.

Modality	RGB	IR	AVG	RGB	IR	AVG	RGB	IR	AVG
Model	AP ₅₀	AP ₅₀	AP ₅₀	AP ₇₅	AP ₇₅	AP ₇₅	AP	AP	AP
Fixed [$\rho=0.25$]	78.9	98.2	88.55	41.5	78.1	59.80	42.5	66.5	54.50
Fixed [$\rho=0.50$]	73.0	97.6	85.30	31.1	78.1	54.60	36.0	67.0	51.50
Fixed [$\rho=0.75$]	77.4	97.5	87.45	40.5	76.5	58.50	42.0	65.2	53.60
Variable	88.5	97.5	93.00	48.9	77.4	63.15	48.9	66.6	57.75
Learnable	69.8	97.0	83.40	26.8	72.7	49.75	32.9	63.4	48.15
Curriculum ($\rho=0.25$ for 8 epochs; then variable)	80.1	97.8	88.95	40.9	79.1	60.00	43.0	67.6	55.30
Curriculum ($\rho=0.25$ for 4 epochs; then variable)	76.6	97.8	87.20	38.0	77.0	57.50	40.7	65.7	53.20

4 Ablation on γ

In this section, we expand our comparison for different γ , in which we provide the full study on different AP metrics. The parameter γ governs the rate at which the modality invariance loss influences training. Thus, for FLIR, the best γ value was 0.05. As shown in the Table 2, we study various values of γ with steps of 0.05, selected following the GRL equation described in our manuscript and inspired by previous works [10]. In this study, the values vary between 0.05 and 0.40, but the values may vary depending on the necessary number of epochs for training, as this function is step-dependent during training. Models that require more epochs may have larger values for γ . On FLIR, MiPa [$\gamma = 0.05$] was able to outperform the other baselines with an average of 67.62 AP₅₀, which is an increase from normal MiPa with 66.52 and the best baseline with 64.72 (BOTH [$\rho = 0.50$]). Moreover, MiPa [$\gamma = 0.05$] reached 29.77 in terms of AP₇₅, which is an average increase from 29.25 of normal MiPa, and 27.45 from the best baseline (BOTH [$\rho = 0.75$]). Note that for such a case, BOTH [$\rho = 0.75$] was better in terms of localization (AP₇₅) in comparison with BOTH [$\rho = 0.50$], even though it is worse than normal MiPa and MiPa with modality agnostic layer. Finally, in terms of

AP, the trend is similar, so on average, we outperform all baselines and normal MiPa, which means that we are better in terms of localization and classification in each modality simultaneously. Thus, in this section, our goal of reaching a better balance between modalities while creating a robust model is successfully achieved.

Table 2: Comparison of detection performance over different baselines and MiPa for different models and backbones. The evaluation is done for RGB, Thermal, and the average of the modalities.

Model Backbone Modality		Test Set (Dataset: FLIR)									
		RGB			Thermal			Average			
		AP ₅₀ ↑	AP ₇₅ ↑	AP ↑	AP ₅₀ ↑	AP ₇₅ ↑	AP ↑	AP ₅₀ ↑	AP ₇₅ ↑	AP ↑	
	RGB	66.07 ± 0.98	27.97 ± 0.22	32.33 ± 0.47	56.60 ± 0.80	20.87 ± 0.56	26.30 ± 0.19	61.33	24.42	29.32	
	THERMAL	56.47 ± 0.79	17.00 ± 0.98	24.30 ± 0.69	70.40 ± 0.38	38.80 ± 0.66	38.97 ± 0.31	63.43	27.90	31.63	
	BOTH [$\rho = 0.25$]	56.53 ± 0.76	18.33 ± 0.55	25.60 ± 0.33	67.57 ± 1.73	31.33 ± 2.10	34.87 ± 1.35	62.05	24.83	30.23	
	BOTH [$\rho = 0.50$]	60.50 ± 0.66	19.60 ± 1.29	27.37 ± 0.58	68.93 ± 0.60	33.03 ± 1.32	35.90 ± 0.82	64.72	26.32	31.63	
	BOTH [$\rho = 0.75$]	58.53 ± 0.92	19.40 ± 0.83	26.47 ± 0.75	70.43 ± 0.65	35.50 ± 1.23	37.53 ± 0.41	64.48	27.45	32.00	
DINO	SWIN	MiPa	63.53 ± 1.94	22.33 ± 0.82	29.47 ± 0.92	69.50 ± 1.84	36.17 ± 0.46	37.57 ± 0.67	66.52	29.25	33.52
		MiPa [$\gamma = 0.05$]	64.80 ± 2.30	24.77 ± 1.05	30.60 ± 0.62	70.43 ± 0.53	34.77 ± 1.18	37.50 ± 0.43	67.62	29.77	34.05
		MiPa [$\gamma = 0.10$]	64.03 ± 2.11	24.10 ± 1.63	30.63 ± 1.22	69.63 ± 1.45	33.13 ± 1.95	36.80 ± 1.39	66.83	28.62	33.72
		MiPa [$\gamma = 0.15$]	64.27 ± 0.47	24.40 ± 0.93	30.07 ± 0.68	69.93 ± 1.02	33.83 ± 1.24	36.80 ± 0.86	67.10	29.12	33.43
		MiPa [$\gamma = 0.20$]	61.83 ± 1.39	22.83 ± 1.01	28.53 ± 0.76	69.27 ± 1.57	31.87 ± 2.02	35.73 ± 1.31	65.55	27.35	32.13
		MiPa [$\gamma = 0.30$]	62.20 ± 2.49	22.93 ± 1.35	29.10 ± 1.28	67.47 ± 2.04	32.53 ± 0.66	35.87 ± 0.69	64.83	27.73	32.48
		MiPa [$\gamma = 0.40$]	61.13 ± 2.88	22.30 ± 0.57	28.50 ± 0.99	67.93 ± 0.92	32.47 ± 0.48	35.87 ± 0.49	64.53	27.38	32.18

5 MiPa on different backbones

In this section, we present additional quantitative results, including the incorporation of KAIST dataset results and various performance metrics measured in terms of different APs. In Table 3, we outline the results obtained using the SWIN backbone for DINO and Deformable DETR across baselines, MiPa, and MiPa with a modality invariance layer. As shown, MiPa demonstrates superior performance compared to using both modalities jointly and other baselines across different datasets. As described in the main manuscript, while MiPa’s compatibility with ConvNexT is not robust, we have included these additional results in Table 4 for completeness.

References

1. Bachmann, R., Mizrahi, D., Atanov, A., Zamir, A.: Multima: Multi-modal multi-task masked autoencoders (2022) 3, 4

Table 3: Comparison of detection performance over different baselines and MiPa for different models and backbones. The evaluation is done for RGB, Thermal, and the average of the modalities.

			Dataset: LLVIP								
Model	Backbone	Modality	RGB			Thermal			Average		
			AP ₅₀ ↑	AP ₇₅ ↑	AP ↑	AP ₅₀ ↑	AP ₇₅ ↑	AP ↑	AP ₅₀ ↑	AP ₇₅ ↑	AP ↑
DINO	SWIN	RGB	90.87 ± 0.84	54.20 ± 1.02	51.87 ± 0.79	94.23 ± 0.57	67.13 ± 0.85	59.43 ± 0.48	92.55	60.67	55.65
		THERMAL	66.87 ± 0.90	20.27 ± 0.98	29.03 ± 0.76	96.87 ± 0.12	73.53 ± 0.40	64.27 ± 0.12	81.87	46.90	46.65
		BOTH [ρ = 0.25]	79.73 ± 1.03	45.70 ± 0.43	44.97 ± 0.33	97.40 ± 0.22	76.03 ± 0.83	65.87 ± 0.45	88.57	60.87	55.42
		BOTH [ρ = 0.50]	82.40 ± 1.50	47.27 ± 1.65	46.43 ± 1.03	96.50 ± 0.29	74.17 ± 2.10	64.83 ± 0.96	89.45	60.72	55.63
		BOTH [ρ = 0.75]	81.23 ± 2.89	45.60 ± 2.49	45.23 ± 2.13	97.07 ± 0.25	74.73 ± 1.41	65.27 ± 0.82	89.15	60.17	55.25
		MiPa (Ours)	88.70 ± 0.45	46.67 ± 0.86	48.00 ± 0.28	96.97 ± 0.26	73.07 ± 1.42	64.30 ± 1.10	92.83	59.87	56.15
		MiPa + MI (Ours)	89.10 ± 0.28	46.60 ± 0.86	48.10 ± 0.33	96.83 ± 0.09	71.17 ± 0.70	63.17 ± 0.58	92.97	58.88	55.63
Def.DETR	SWIN	RGB	80.00 ± 1.50	35.50 ± 0.22	40.27 ± 0.41	90.03 ± 0.87	50.37 ± 0.85	49.67 ± 0.48	85.02	42.93	44.97
		THERMAL	56.10 ± 2.50	10.77 ± 1.47	21.10 ± 1.34	94.20 ± 0.08	62.20 ± 0.86	56.73 ± 0.47	75.15	36.48	38.92
		BOTH [ρ = 0.25]	51.20 ± 3.47	22.57 ± 1.96	25.70 ± 1.91	83.73 ± 16.57	54.17 ± 16.62	48.30 ± 14.93	67.47	38.37	37.00
		BOTH [ρ = 0.50]	53.57 ± 4.17	23.13 ± 2.15	26.57 ± 2.11	83.87 ± 16.17	52.67 ± 17.17	49.37 ± 12.64	68.72	37.90	37.97
		BOTH [ρ = 0.75]	53.53 ± 4.55	22.83 ± 2.72	26.5 ± 2.63	82.33 ± 18.48	51.33 ± 18.56	48.13 ± 14.03	67.93	37.08	37.32
		MiPa (Ours)	78.60 ± 0.42	23.33 ± 5.85	29.20 ± 6.37	95.20 ± 0.16	62.60 ± 0.78	56.80 ± 0.45	86.90	42.97	43.00
		MiPa + MI (Ours)	79.02 ± 0.21	24.36 ± 2.85	31.25 ± 4.32	95.36 ± 0.25	63.38 ± 0.43	57.25 ± 0.43	87.19	43.87	44.25
			Dataset: FLIR								
Model	Backbone	Modality	RGB			Thermal			Average		
			AP ₅₀ ↑	AP ₇₅ ↑	AP ↑	AP ₅₀ ↑	AP ₇₅ ↑	AP ↑	AP ₅₀ ↑	AP ₇₅ ↑	AP ↑
DINO	SWIN	RGB	66.07 ± 0.98	27.97 ± 0.22	32.33 ± 0.47	56.60 ± 0.80	20.87 ± 0.56	26.30 ± 0.19	61.33	24.42	29.32
		THERMAL	56.47 ± 0.79	17.00 ± 0.98	24.30 ± 0.69	70.40 ± 0.38	38.80 ± 0.66	38.97 ± 0.31	63.43	27.90	31.63
		BOTH [ρ = 0.25]	56.53 ± 0.76	18.33 ± 0.55	25.60 ± 0.33	67.57 ± 1.73	31.33 ± 2.10	34.87 ± 1.35	62.05	24.83	30.23
		BOTH [ρ = 0.50]	60.50 ± 0.66	19.60 ± 1.29	27.37 ± 0.58	68.93 ± 0.60	33.03 ± 1.32	35.90 ± 0.82	64.72	26.32	31.63
		BOTH [ρ = 0.75]	58.53 ± 0.92	19.40 ± 0.83	26.47 ± 0.75	70.43 ± 0.65	35.50 ± 1.23	37.53 ± 0.41	64.48	27.45	32.00
		MiPa (Ours)	63.53 ± 1.94	22.33 ± 0.82	29.47 ± 0.92	69.50 ± 1.84	36.17 ± 0.46	37.57 ± 0.67	66.52	29.25	33.52
		MiPa + MI (Ours)	64.80 ± 2.30	24.77 ± 1.05	30.60 ± 0.62	70.43 ± 0.53	34.77 ± 1.18	37.50 ± 0.43	67.62	29.77	34.05
Def.DETR	SWIN	RGB	49.33 ± 1.39	13.93 ± 0.30	20.97 ± 0.53	43.77 ± 0.56	10.13 ± 0.08	17.37 ± 0.19	46.55	12.03	19.17
		THERMAL	39.17 ± 1.48	08.57 ± 0.24	14.90 ± 0.50	59.20 ± 0.29	20.03 ± 0.33	26.93 ± 0.62	49.18	14.30	20.92
		BOTH [ρ = 0.25]	35.73 ± 4.95	08.27 ± 1.51	14.00 ± 2.38	43.00 ± 13.54	14.30 ± 5.97	19.23 ± 7.01	39.37	11.28	16.62
		BOTH [ρ = 0.50]	33.93 ± 5.15	08.23 ± 1.43	13.60 ± 2.17	43.33 ± 14.14	14.70 ± 6.34	19.63 ± 7.43	38.63	11.47	16.62
		BOTH [ρ = 0.75]	32.90 ± 3.54	07.70 ± 1.20	12.97 ± 1.65	44.13 ± 14.85	14.17 ± 6.30	19.47 ± 7.37	38.52	10.93	16.22
		MiPa (Ours)	48.00 ± 0.57	15.23 ± 0.69	20.70 ± 0.45	54.97 ± 0.90	19.80 ± 0.28	25.50 ± 0.42	51.48	17.52	23.10
		MiPa + MI (Ours)	48.27 ± 1.76	14.57 ± 1.05	20.63 ± 0.96	55.80 ± 0.22	21.00 ± 0.67	26.33 ± 0.39	52.03	17.78	23.48
			Dataset: KAIST								
Model	Backbone	Modality	RGB			Thermal			Average		
			AP ₅₀ ↑	AP ₇₅ ↑	AP ↑	AP ₅₀ ↑	AP ₇₅ ↑	AP ↑	AP ₅₀ ↑	AP ₇₅ ↑	AP ↑
DINO	SWIN	RGB	46.50 ± 0.05	36.67 ± 0.56	30.50 ± 0.12	35.37 ± 0.28	14.87 ± 0.57	17.43 ± 0.29	40.93	25.77	23.97
		THERMAL	23.73 ± 0.89	10.70 ± 0.45	11.53 ± 0.36	49.30 ± 0.41	38.33 ± 0.39	31.73 ± 0.12	36.52	24.52	21.63
		BOTH [ρ = 0.25]	37.30 ± 0.76	23.13 ± 0.78	21.63 ± 0.28	43.23 ± 0.08	22.10 ± 0.29	23.30 ± 0.17	40.27	22.62	22.47
		BOTH [ρ = 0.50]	36.80 ± 0.97	22.57 ± 0.70	21.30 ± 0.48	46.37 ± 0.82	28.87 ± 3.06	27.20 ± 1.36	41.58	25.72	24.25
		BOTH [ρ = 0.75]	36.33 ± 0.74	22.03 ± 1.19	20.63 ± 0.74	47.37 ± 0.39	32.27 ± 0.90	28.73 ± 0.72	41.85	27.15	24.68
		MiPa (Ours)	39.50 ± 0.86	22.93 ± 1.34	22.40 ± 1.03	46.60 ± 1.80	27.67 ± 4.00	26.63 ± 2.10	43.05	25.30	24.52
		MiPa + MI (Ours)	39.36 ± 1.76	25.88 ± 1.02	23.76 ± 0.72	46.04 ± 0.34	27.19 ± 0.26	27.80 ± 0.08	42.70	26.53	25.78

Table 4: Comparison of detection performance over different baselines and MiPa for different models and backbones. The evaluation is done for RGB, Thermal, and the average of the modalities.

			Dataset: LLVIP								
Model	Backbone	Modality	RGB			Thermal			Average		
			AP ₅₀ ↑	AP ₇₅ ↑	AP ↑	AP ₅₀ ↑	AP ₇₅ ↑	AP ↑	AP ₅₀ ↑	AP ₇₅ ↑	AP ↑
DINO	ConvNeXt	RGB	90.77 ± 0.34	47.13 ± 3.07	48.83 ± 1.31	92.20 ± 0.62	51.43 ± 3.36	51.10 ± 1.58	91.48	49.28	49.97
		THERMAL	63.23 ± 9.02	14.20 ± 2.83	24.97 ± 4.21	95.60 ± 0.45	69.90 ± 2.73	61.30 ± 1.28	79.42	42.05	43.13
		BOTH [$\rho = 0.25$]	76.70 ± 4.04	35.07 ± 2.68	39.30 ± 2.17	96.27 ± 0.48	67.00 ± 4.14	59.83 ± 1.96	86.48	51.03	49.57
		BOTH [$\rho = 0.50$]	81.40 ± 2.55	42.40 ± 2.04	43.70 ± 1.53	95.50 ± 0.57	68.77 ± 2.29	60.67 ± 1.17	88.45	55.58	52.18
		BOTH [$\rho = 0.75$]	79.80 ± 1.49	41.40 ± 1.36	42.93 ± 0.77	95.60 ± 0.57	70.83 ± 2.53	61.80 ± 0.73	87.70	56.12	52.37
		MiPa (Ours)	81.03 ± 0.74	37.40 ± 2.70	41.53 ± 1.19	96.43 ± 0.12	71.23 ± 1.33	62.83 ± 0.56	88.73	54.32	52.18
			Dataset: FLIR								
Model	Backbone	Modality	RGB			Thermal			Average		
			AP ₅₀ ↑	AP ₇₅ ↑	AP ↑	AP ₅₀ ↑	AP ₇₅ ↑	AP ↑	AP ₅₀ ↑	AP ₇₅ ↑	AP ↑
DINO	ConvNeXt	RGB	52.77 ± 1.43	17.87 ± 1.49	23.57 ± 1.12	48.33 ± 1.87	11.90 ± 0.54	18.90 ± 0.21	50.55	14.88	21.23
		THERMAL	39.43 ± 0.39	10.63 ± 0.15	16.10 ± 0.22	58.87 ± 0.87	23.20 ± 0.29	28.23 ± 0.04	49.15	16.92	22.17
		BOTH [$\rho = 0.25$]	45.87 ± 1.14	12.17 ± 0.20	18.93 ± 0.53	54.53 ± 1.20	20.77 ± 0.85	26.17 ± 0.86	50.20	16.47	22.55
		BOTH [$\rho = 0.50$]	48.00 ± 2.87	14.33 ± 1.59	20.93 ± 2.08	55.40 ± 0.05	22.43 ± 0.48	26.77 ± 0.43	51.70	18.38	23.85
		BOTH [$\rho = 0.75$]	52.97 ± 3.03	14.17 ± 0.42	22.57 ± 0.54	57.53 ± 0.86	23.33 ± 0.45	28.10 ± 0.29	55.25	18.75	25.33
		MiPa (Ours)	46.17 ± 0.66	15.73 ± 0.40	20.57 ± 0.30	56.27 ± 0.33	23.47 ± 0.07	28.03 ± 0.10	51.22	19.60	24.30
DefDETR	ConvNeXt	RGB	50.17 ± 1.07	10.80 ± 0.52	19.30 ± 0.31	44.53 ± 1.09	07.90 ± 0.22	16.20 ± 0.70	47.35	09.35	17.75
		THERMAL	36.87 ± 0.63	7.27 ± 0.25	13.77 ± 0.36	56.37 ± 1.75	17.20 ± 0.85	23.73 ± 0.57	46.62	12.23	18.75
		BOTH [$\rho = 0.25$]	33.23 ± 4.29	6.60 ± 1.40	11.97 ± 2.01	44.73 ± 13.78	11.57 ± 4.24	18.33 ± 6.31	38.98	09.08	15.15
		BOTH [$\rho = 0.50$]	32.60 ± 5.19	6.43 ± 0.91	12.43 ± 1.72	46.83 ± 13.52	12.00 ± 4.45	18.97 ± 6.60	39.72	09.22	15.70
		BOTH [$\rho = 0.75$]	31.60 ± 5.00	6.37 ± 1.03	11.80 ± 2.05	42.83 ± 12.68	12.00 ± 4.81	18.00 ± 6.17	37.22	09.18	14.90
		MiPa (Ours)	34.55 ± 3.12	8.27 ± 0.95	12.25 ± 2.35	44.53 ± 7.45	13.23 ± 3.45	19.84 ± 4.56	39.54	10.75	16.04
			Dataset: KAIST								
Model	Backbone	Modality	RGB			Thermal			Average		
			AP ₅₀ ↑	AP ₇₅ ↑	AP ↑	AP ₅₀ ↑	AP ₇₅ ↑	AP ↑	AP ₅₀ ↑	AP ₇₅ ↑	AP ↑
DINO	ConvNeXt	RGB	37.40 ± 0.83	18.80 ± 0.29	20.10 ± 0.46	19.67 ± 0.51	03.63 ± 0.16	07.47 ± 0.16	28.53	11.22	13.78
		THERMAL	11.10 ± 0.54	02.77 ± 0.54	04.40 ± 0.50	43.30 ± 0.29	23.83 ± 0.38	23.70 ± 0.22	27.20	13.30	14.05
		BOTH [$\rho = 0.25$]	25.47 ± 1.35	08.37 ± 0.81	10.90 ± 0.80	31.53 ± 3.70	08.60 ± 2.98	13.13 ± 2.65	28.50	08.48	12.02
		BOTH [$\rho = 0.50$]	36.80 ± 0.97	22.57 ± 0.70	21.30 ± 0.48	46.37 ± 0.82	28.87 ± 3.06	27.20 ± 1.36	41.58	25.72	24.25
		BOTH [$\rho = 0.75$]	27.27 ± 2.11	11.73 ± 2.95	13.57 ± 1.78	34.63 ± 7.91	27.10 ± 11.17	21.90 ± 2.42	30.95	19.42	17.73
		MiPa (Ours)	24.20 ± 0.80	8.33 ± 0.34	10.80 ± 0.36	31.63 ± 0.83	11.23 ± 0.53	14.43 ± 0.67	27.92	09.78	12.62

2. Baltrušaitis, T., Ahuja, C., Morency, L.P.: Multimodal machine learning: A survey and taxonomy. *IEEE transactions on pattern analysis and machine intelligence* **41**(2), 423–443 (2018) [3](#)
3. Bayouh, K., Knani, R., Hamdaoui, F., Mtibaa, A.: A survey on deep multimodal learning for computer vision: advances, trends, applications, and datasets. *The Visual Computer* **38**, 2939–2970 (2021), <https://api.semanticscholar.org/CorpusID:235410640> [4](#)
4. Cao, Y., Bin, J., Hamari, J., Blasch, E., Liu, Z.: Multimodal object detection by channel switching and spatial attention. In: 2023 IEEE/CVF Conference on Computer Vision and Pattern Recognition Workshops (CVPRW). pp. 403–411 (2023). <https://doi.org/10.1109/CVPRW59228.2023.00046> [2, 4, 8, 13, 14](#)
5. Chen, J., Li, K., Deng, Q., Li, K., Philip, S.Y.: Distributed deep learning model for intelligent video surveillance systems with edge computing. *IEEE Transactions on Industrial Informatics* (2019) [1](#)
6. Chen, Y.T., Shi, J., Ye, Z., Mertz, C., Ramanan, D., Kong, S.: Multimodal object detection via probabilistic ensembling (2022) [2, 4, 13, 14](#)
7. Das, A., Das, S., Sistu, G., Horgan, J., Bhattacharya, U., Jones, E., Glavin, M., Eising, C.: Revisiting modality imbalance in multimodal pedestrian detection (2023) [3, 4](#)
8. Dosovitskiy, A., Beyer, L., Kolesnikov, A., Weissenborn, D., Zhai, X., Unterthiner, T., Dehghani, M., Minderer, M., Heigold, G., Gelly, S., Uszkoreit, J., Houlsby, N.: An image is worth 16x16 words: Transformers for image recognition at scale. *CoRR* **abs/2010.11929** (2020), <https://arxiv.org/abs/2010.11929> [3, 4](#)
9. Du, C., Li, T., Liu, Y., Wen, Z., Hua, T., Wang, Y., Zhao, H.: Improving multi-modal learning with uni-modal teachers (2021) [5](#)
10. Ganin, Y., Lempitsky, V.: Unsupervised domain adaptation by backpropagation (2015) [8, 18](#)
11. He, K., Chen, X., Xie, S., Li, Y., Dollár, P., Girshick, R.: Masked autoencoders are scalable vision learners. In: Proceedings of the IEEE/CVF conference on computer vision and pattern recognition. pp. 16000–16009 (2022) [3, 4](#)
12. Kong, X., Ge, Z.: Deep learning of latent variable models for industrial process monitoring. *IEEE Transactions on Industrial Informatics* **18**(10), 6778–6788 (2021) [1](#)
13. Lin, T.Y., Maire, M., Belongie, S., Bourdev, L., Girshick, R., Hays, J., Perona, P., Ramanan, D., Zitnick, C.L., Dollár, P.: Microsoft coco: Common objects in context (2015) [4](#)
14. Liu, Z., Lin, Y., Cao, Y., Hu, H., Wei, Y., Zhang, Z., Lin, S., Guo, B.: Swin transformer: Hierarchical vision transformer using shifted windows (2021) [4](#)
15. Liu, Z., Mao, H., Wu, C., Feichtenhofer, C., Darrell, T., Xie, S.: A convnet for the 2020s. *CoRR* **abs/2201.03545** (2022), <https://arxiv.org/abs/2201.03545> [4, 10](#)
16. Loshchilov, I., Hutter, F.: Decoupled weight decay regularization. *arXiv preprint arXiv:1711.05101* (2017) [9](#)
17. Pawłowski, M., Wróblewska, A., Sysko-Romańczuk, S.: Effective techniques for multimodal data fusion: A comparative analysis. *Sensors* **23**(5) (2023). <https://doi.org/10.3390/s23052381>, <https://www.mdpi.com/1424-8220/23/5/2381> [4](#)
18. Peng, X., Wei, Y., Deng, A., Wang, D., Hu, D.: Balanced multimodal learning via on-the-fly gradient modulation. In: 2022 IEEE/CVF Conference on Computer Vision and Pattern Recognition (CVPR). pp. 8228–8237 (2022). <https://doi.org/10.1109/CVPR52688.2022.00806> [5](#)
19. Pierson, H.A., Gashler, M.S.: Deep learning in robotics: a review of recent research. *Advanced Robotics* **31**(16), 821–835 (2017) [1](#)
20. Qingyun, F., Dapeng, H., Zhaokui, W.: Cross-modality fusion transformer for multispectral object detection. *arXiv preprint arXiv:2111.00273* (2021) [14](#)
21. Russakovsky, O., Deng, J., Su, H., Krause, J., Satheesh, S., Ma, S., Huang, Z., Karpathy, A., Khosla, A., Bernstein, M.S., Berg, A.C., Fei-Fei, L.: Imagenet large scale visual recognition

- challenge. CoRR **abs/1409.0575** (2014), <http://arxiv.org/abs/1409.0575> **4, 9, 10**
22. Stilgoe, J.: Machine learning, social learning and the governance of self-driving cars. *Social studies of science* **48**(1), 25–56 (2018) **1**
 23. Tang, Q., Liang, J., Zhu, F.: A comparative review on multi-modal sensors fusion based on deep learning. *Signal Processing* p. 109165 (2023) **2**
 24. Touvron, H., Cord, M., Douze, M., Massa, F., Sablayrolles, A., Jégou, H.: Training data-efficient image transformers & distillation through attention. CoRR **abs/2012.12877** (2020), <https://arxiv.org/abs/2012.12877> **4**
 25. Wagner, J., Fischer, V., Herman, M., Behnke, S.: Multispectral pedestrian detection using deep fusion convolutional neural networks (04 2016) **2, 9**
 26. Wang, Q., Chi, Y., Shen, T., Song, J., Zhang, Z., Zhu, Y.: Improving rgb-infrared object detection by reducing cross-modality redundancy. *Remote Sensing* **14**(9), 2020 (2022) **2**
 27. Wang, W., Tran, D., Feiszli, M.: What makes training multi-modal classification networks hard? In: 2020 IEEE/CVF Conference on Computer Vision and Pattern Recognition (CVPR). pp. 12692–12702 (2020). <https://doi.org/10.1109/CVPR42600.2020.012715> **5**
 28. Woo, S., Debnath, S., Hu, R., Chen, X., Liu, Z., Kweon, I.S., Xie, S.: Convnext v2: Co-designing and scaling convnets with masked autoencoders (2023) **4**
 29. Yuan, L., Hou, Q., Jiang, Z., Feng, J., Yan, S.: VOLO: vision outlooker for visual recognition. CoRR **abs/2106.13112** (2021), <https://arxiv.org/abs/2106.13112> **4**
 30. Zhang, H., Li, F., Liu, S., Zhang, L., Su, H., Zhu, J., Ni, L.M., Shum, H.Y.: Dino: Detr with improved denoising anchor boxes for end-to-end object detection (2022) **4**
 31. Zhang, H., Fromont, E., Lefèvre, S., Avignon, B.: Multispectral fusion for object detection with cyclic fuse-and-refine blocks. In: 2020 IEEE International Conference on Image Processing (ICIP). pp. 276–280. IEEE (2020) **8, 13, 14**
 32. Zhang, H., Fromont, E., Lefevre, S., Avignon, B.: Multispectral fusion for object detection with cyclic fuse-and-refine blocks. In: 2020 IEEE International Conference on Image Processing (ICIP). pp. 276–280 (2020). <https://doi.org/10.1109/ICIP40778.2020.9191080> **2, 4, 9**
 33. ZHANG, H., FROMONT, E., LEFEVRE, S., AVIGNON, B.: Guided attentive feature fusion for multispectral pedestrian detection. In: 2021 IEEE Winter Conference on Applications of Computer Vision (WACV). pp. 72–80 (2021). <https://doi.org/10.1109/WACV48630.2021.00012> **2, 4, 9, 13, 14**